THE JOURNAL OF PHYSICAL CHEMISTRY LETTERS
A JOURNAL OF THE AMERICAN CHEMICAL SOCIETY

pubs.acs.org/JPCL

Letter

Common Defects Accelerate Charge Carrier Recombination in $CsSnI_3$ without Creating Mid-Gap States

Yifan Wu, Weibin Chu, Andrey S. Vasenko, and Oleg V. Prezhdo*

Cite This: *J. Phys. Chem. Lett.* 2021, 12, 8699–8705

Read Online

ACCESS | Metrics & More | Article Recommendations | Supporting Information

ABSTRACT: Lead-free metal halide perovskites are environmentally friendly and have favorable electro-optical properties; however, their efficiencies are significantly below the theoretical limit. Using ab initio nonadiabatic molecular dynamics, we show that common intrinsic defects accelerate nonradiative charge recombination in $CsSnI_3$ without creating midgap traps. This is in contrast to Pb-based perovskites, in which many defects have little influence on and even prolong carrier lifetimes. Sn-related defects, such as Sn vacancies and replacement of Sn with Cs are most detrimental, since Sn removal breaks the largest number of bonds and strongly perturbs the Sn−I lattice that supports the carriers. The defects increase the nonadiabatic electron-vibrational coupling and interact strongly with free carrier states. Point defects associated with I atoms are less detrimental, and therefore, $CsSnI_3$ synthesis should be performed in Sn rich conditions. The study provides an atomistic rationalization of why lead-free $CsSnI_3$ exhibits lower photovoltaic efficiency compared to some lead-based perovskites.

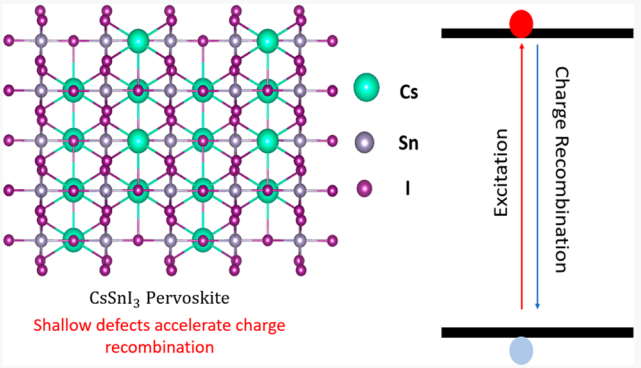

As one of the most rapidly growing photovoltaic devices, metal halide perovskite (MHP) solar cells convert solar energy to electricity[1] and chemical fuels[2] and are regarded as a promising technology due to ease of fabrication and high power conversion efficiency (PCE) that has reached 25.5%.[3] Extensive studies have been performed to investigate MHPs, which show many favorable and unique properties, such as long electron and hole diffusion,[4,5] high charge carrier mobility,[6,7] high optical absorption,[8,9] and bandgap tunning over a wide energy range.[10,11] Due to the outstanding photoelectric properties and low cost to produce,[12] MHPs have attracted much attention for optoelectronic device applications, including solar cells,[1,2] light-emitting diodes,[13] photodetectors,[14] sensors,[15] etc. Although MHPs have excellent optoelectronic performance, several issues remain to be solved, such as stability upon exposure to humidity[16,17] and the toxicity of lead.

Due to the toxicity of lead and demands for clean and renewable energy, lead-free tin-based MHPs intrigue a considerable number of researchers, as they are more environmentally friendly than lead-based perovskites.[18−25] It would be desirable to find replacements of the Pb cation, keeping the superior optoelectronic properties of lead-halide perovskites. Intuitively, group 14 metals, such as Sn or Ge, constitute the first choice, especially since the very first fabricated organic−inorganic halide perovskites for optoelectronic applications were based on Sn.[26] $CsSnI_3$ was successfully fabricated and tested in 2010.[27] In 2012, $CsSnI_3$ was reported to serve as a hole-transporter in dye-sensitized solar cells.[28] The organic−inorganic Sn-based halide perovskite $CH_3NH_3SnI_3$ was demonstrated to achieve a PCE of 6.4%.[29] Further, to stabilize Sn-based perovskites, double perovskite with the A_2SnX_6 composition were fabricated, such as Cs_2SnX_6.[30] However, compared to B-γ $CsSnI_3$, Cs_2SnX_6 has a much poorer light-harvesting ability, coming from the undesired oxidation of Sn^{2+}.[31−33] Acting as the light absorber material in solar cells, $CsSnI_3$ achieved the highest PCE of 10.1%.[34] $CsSnI_3$ can exist independently in the double-chain structure (Y) and the three-dimensional perovskite structure (B-γ), at room temperature. Here, we focus on B-γ $CsSnI_3$, which has a direct bandgap[35] of ∼1.3 eV, placing it in the favorable bandgap range with the theoretical limit of the PCE of ∼33% for single junction devices.[31,36,37] The large difference between the measured (∼10%) and theoretical (>30%) efficiencies suggests that there exist significant pathways for charge and energy losses. The losses are predominantly nonradiative, occur via charge trapping and electron−hole (e−h) recombination, and require a mechanistic under-

Received: July 27, 2021
Accepted: August 30, 2021
Published: September 2, 2021

https://doi.org/10.1021/acs.jpclett.1c02443
J. Phys. Chem. Lett. 2021, 12, 8699–8705

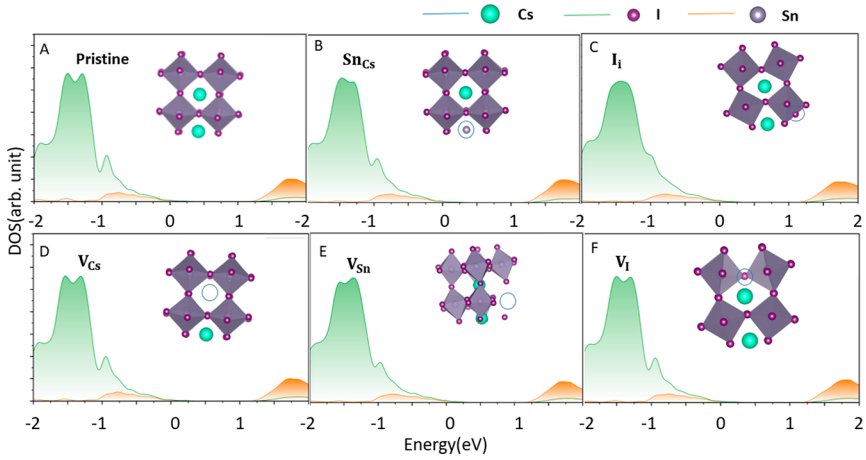

Figure 1. (A to F) Element-projected density of states (DOS) of pristine and defective $CsSnI_3$. The insets show the corresponding structures, with blue circles indicating defect locations. The energy reference is set at the VBM. DOS of the defect sites are shown in Figure S1.

standing.[38,39] Solution-based fabrication of MHPs at room temperature inevitably introduces various defects. Lead-based perovskites, such as $CsPbI_3$ and $MAPbI_3$, exhibit strong defect tolerance.[40−42] Compared to the lead-based perovskites, tin-based perovskites exhibit a relatively poorer PCE. Therefore, a comprehensive understanding and investigation of the changes in the electronic properties and charge carrier losses induced by defects in tin-based perovskites is strongly needed.

We consider intrinsic point defects in $CsPbI_3$, particularly those with relatively low formation energies, Figure 1. These are the three types of vacancies (V_{Cs}, V_{Sn}, and V_I), the most common interstitial defect (I_i), and the antisite defect (Sn_{Cs}), in which Sn is substituted by Cs.[43] The investigated defects introduce no midgap trap states. However, the nonradiative charge recombination is accelerated in all defective B-γ $CsSnI_3$ systems, showing inferior defect tolerance compared to the Pb-based analog. Missing Sn atoms are most detrimental for the carrier lifetime, indicating that $CsSnI_3$ synthesis should be carried out in Sn rich conditions.

We employ ab initio nonadiabatic molecular dynamics (NA-MD) using the Pyxaid package[44,45] to investigate the nonradiative charge trapping and recombination in pristine and defective $CsSnI_3$. We use the decoherence induced surface hopping (DISH) method[46] under the classical path approximation.[45,47] The ion cores are treated classically due to their heavier and slower nature, while the electrons are described quantum mechanically with real-time time-dependent density functional theory. DISH incorporates decoherence into the quantum-classical dynamics simulation. This is vital because decoherence time is much shorter than the charge carrier lifetime. The decoherence effect should be considered when simulating e−h recombination. The decoherence time is estimated by computing the pure-dephasing time via the second-order cumulant approximation of the optical response theory.[48−50]

The geometry optimization, adiabatic MD, densities of states (DOS), and orbital spatial distributions are obtained with the Vienna Ab initio Simulation Package (VASP).[51] The Perdew−Burke−Ernzerhof (PBE) exchange−correlation functional is used.[52] The interactions between the electrons and the ion cores are described by the projected-augmented wave method (PAW).[53] A large simulation cell is employed, composed of 2 × 4 × 4 unit cells and containing 160 atoms in total. The plane-wave basis energy cutoff is set to 350 eV. A 3 × 3 × 2 Γ-centered k-point Monkhorst−Pack mesh is used for geometry optimization. The electronic properties are calculated with a denser Γ-centered k-point grid of 5 × 5 × 5 to obtain more accurate results. Adiabatic MD simulations are performed at the Γ-point only for computational efficiency, because the simulation cell is large and composed of 32 unit cells, and because $CsSnI_3$ is a direct bandgap semiconductor with the conduction and valence band edges located at the Γ-point. Geometry is optimized first. Then, all systems are heated to 300 K by repeated velocity rescaling to reach thermal equilibrium in a canonical ensemble. After that, 9 ps adiabatic MD trajectories are obtained in a microcanonical ensemble with a 1 fs atomic time step. The nonadiabatic couplings (NACs) are calculated using the CA-NAC package,[54,55] considering the overlap of two wave functions at adjacent timesteps.[56]

$$
\begin{aligned}
\mathbf{d}_{ji} &= -\mathrm{i}\hbar\langle\varphi_j(\mathbf{r}, \mathbf{R}(t))|\nabla_R|\varphi_i(\mathbf{r}, \mathbf{R}(t))\rangle \frac{\mathrm{d}\mathbf{R}}{\mathrm{d}t} \\
&= -\mathrm{i}\hbar\frac{\langle\varphi_j(\mathbf{r}, \mathbf{R}(t))|\nabla_R H(\mathbf{R}(t))|\varphi_i(\mathbf{r}, \mathbf{R}(t))\rangle}{E_i - E_j}\frac{\mathrm{d}\mathbf{R}}{\mathrm{d}t} \\
&= -\mathrm{i}\hbar\langle\varphi_j(\mathbf{r}, \mathbf{R}(t))|\frac{\partial}{\partial t}|\varphi_i(\mathbf{r}, \mathbf{R}(t))\rangle \\
&\approx -\frac{\mathrm{i}\hbar}{2\Delta t}(\langle\varphi_j(t)|\varphi_i(t+\Delta t)\rangle - \langle\varphi_j(t+\Delta t)|\varphi_i(t)\rangle)
\end{aligned}
\tag{1}
$$

Electronic structure calculations are performed first for all defective and pristine systems, showing that these intrinsic point defects do not introduce deep midgap trap states. Figure 1 demonstrates the calculated element-projected DOS of pristine $CsSnI_3$ and that containing defects at 0 K, with the insets showing the optimized structures. Previous studies show that defects of lead-based perovskites, such as $CsPbI_3$ and $MAPbI_3$, usually introduce deep midgap and shallow defect states near the conduction band minimum (CBM) or the valence band maximum (VBM).[40,57−59] In comparison, the considered defects of tin-based $CsSnI_3$ introduce states inside the bands and no deep midgap trap states, indicating that no e−h recombination centers are created by these intrinsic defects. Further, some of the defects of the lead-based perovskites cause suppression of e−h recombination, resulting in longer charge carrier lifetimes and showing good defect

https://doi.org/10.1021/acs.jpclett.1c02443
J. Phys. Chem. Lett. 2021, 12, 8699−8705

tolerance.[40−42] In comparison, $CsSnI_3$ behaves in the opposite way. All studied intrinsic point defects of $CsSnI_3$ demonstrate accelerations of e−h recombination, consequently, decreasing the PCE.

Figure 1 demonstrates that atomic orbitals of Sn contribute most to the conduction band, while iodine orbitals contribute most to the valence band. Almost no contributions from Cs atoms are seen to either band, meaning that Cs atoms do not directly participate in the charge generation and recombination processes. I_i and V_{Cs} introduce shallow defect states near the VBM. The defect state of V_{Sn} is deep inside the valence band. I_i, V_{Sn}, and V_{Cs} are regarded as p-type defects. V_i introduces defect states near the CBM, while Sn_{Cs} introduces a deep defect state inside the CBM. Both V_i and Sn_{Cs} are regarded as n-type defects. DOS of the defect sites are shown in Figure S1 of the Supporting Information (SI).

Figure 2 presents spatial distribution for the frontier orbitals of the pristine and defective systems. In the pristine system, Figure 2(A), the VBM is distributed on iodine atoms, while the CBM is distributed on Sn mainly, which is in good agreement with the previous first-principles study,[60] and with the calculated DOS, Figure 1. For both pristine and defective systems, the VBM and the CBM are delocalized over the whole simulation cell, with exception of the VBM for I_i, Figure 2(E), and the CBM for V_{Sn}, Figure 2(F), which are localized away from the defects.

To characterize the phonon modes that couple to the electronic subsystem during the nonradiative e−h recombination, we compute Fourier transforms (FTs) of the autocorrelation functions of the NACs, Figure 3, and the CBM-VBM energy gaps, Figure S2 of the Supporting Information. Known as the spectral densities and influence spectra, the NAC FTs identify the phonon modes involved in inelastic scattering, and the energy gap FTs identify the modes participating in the elastic scattering.[48−50] The intensity for a particular frequency seen in the FTs characterize the coupling of the vibrational motion of that frequency to the electronic subsystem. Figure 3 demonstrates that in pristine $CsSnI_3$ phonons with relatively higher frequencies are actively participating in the coupling to the electronic subsystems. In comparison, phonon modes of lower frequencies generate the stronger signals in the systems with the defects. The larger amplitudes of the signals seen in the influence spectra of the defective $CsSnI_3$ systems correlate with the larger NAC, Table 1. The low frequency modes are associated with heavy atoms that have relatively slower atomic velocities, possibly contributed by the Sn−I lattice. After introduction of the intrinsic defects, the influence spectra are red-shifted. The dominant phonon modes are below 100 cm^{-1}. The low-frequency modes at 20−30 cm^{-1} can be attributed to motions of the heavy Cs atoms and shaking of the SnI_6 octahedral cages.[61] Further, the peak around 70 cm^{-1} can originate from hindered translational motion of the atoms.[62] The Sn−I bending contributes to the phonon modes at 100−110 cm^{-1}, while the peak around 150 cm^{-1} can be interpreted as the Sn−I stretching[63] that give has the gives the largest contribution to the NA electron−phonon coupling[64] in the pristine system, Figure 3(A).

Figure S2 of the Supporting Information shows FTs of the energy gaps of the pristine and defective systems. Compared to the NAC FTs, Figure 3, the gap FTs exhibit fewer phonon frequencies, and the active modes reside in the lower frequency range. This is because the NAC is more sensitive to changes in the electronic wave functions caused by atomic motions than the energy gap. Therefore, a wider range of atomic motions contribute to the NAC than to the energy gap fluctuation. Slight blue shifts are found in the energy gap FTs of the defective systems, except for V_I. FTs of the energy gaps of $CsSnI_3$ with the intrinsic point defects have higher amplitudes, in particular for the vacancies V_{Sn} and V_I of the elements contributing to the CBM and the VBM, Figure S2. As a result, the coherence times for the CBM-VBM transitions are shorter, Table 1, since the pure-dephasing time is inversely proportional to the energy gap fluctuation.[48,65] The energy gap fluctuation becomes larger and decoherence accelerates upon introduction of the point defects because the inorganic lattice Sn−I, supporting both the VBM and the CBM, becomes softer and less ordered.

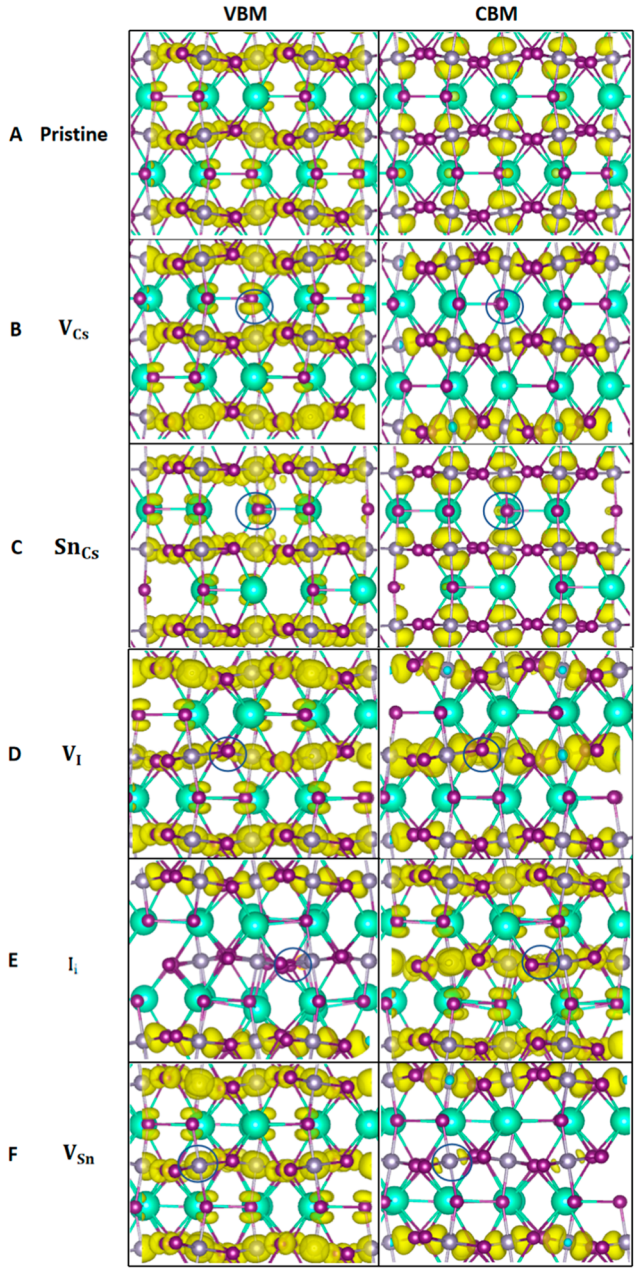

Figure 2. VBM and CBM charge densities of (A to F) pristine and defective $CsSnI_3$, with the blue circles indicating the defect locations.

https://doi.org/10.1021/acs.jpclett.1c02443
J. Phys. Chem. Lett. 2021, 12, 8699−8705

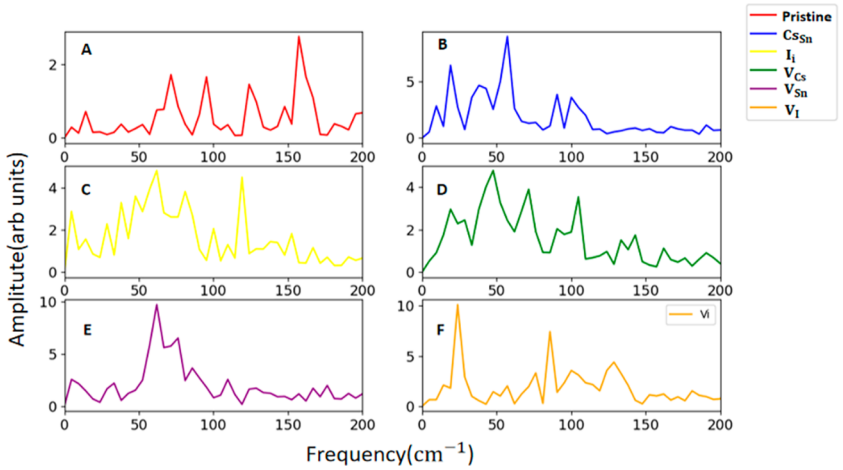

Figure 3. Fourier transforms of the autocorrelation function of NACs in (A to F) pristine and defective $CsSnI_3$. The corresponding data for the bandgaps are shown in Figure S2.

Table 1. Root-Mean-Square (rms) NAC, Average Absolute (abs) NAC, Pure-Dephasing Time, Average Absolute Atomic Velocity, and Recombination Time for the Pristine and Defective Systems

	rmsNAC (meV)	absNAC (meV)	dephasing (fs)	velocity (Å/fs)	recombination (ns)
pristine	0.077	0.063	18.29	0.00220	98.0
Sn_{Cs}	0.102	0.082	13.64	0.00226	40.0
I_i	0.108	0.087	15.13	0.00224	50.8
V_{Cs}	0.104	0.085	14.12	0.00231	62.1
V_{Sn}	0.119	0.094	14.52	0.00233	30.8
V_I	0.119	0.093	12.69	0.00228	82.9

The nonradiative e−h recombination is governed by the electronic energy gap, the NAC, and quantum coherence between the initial and final states.[66−77] The $CsSnI_3$ bandgap obtained in the calculation, Figure 1, agrees with the experimental value[35] of 1.3 eV. The defects introduce little change to the bandgap. At the same time, the defects increase the NAC, as demonstrated by the canonically averaged absolute and root-mean-square NAC values, Table 1. The increased NAC accelerates the nonradiative charge carrier recombination. The NAC growth correlates with the faster average absolute atomic velocities in the defective systems, also presented in Table 1, since the NAC is directly proportional to the velocity, eq 1. The NAC, as well as the velocity, are the largest in the V_{Sn} system, because the Sn vacancy breaks several bonds in the Sn−I inorganic lattice, increasing atomic fluctuations. Note that the amplitudes of the FTs of the bandgap, Figure S2, and the NAC, Figure 3, are also the largest for the V_{Sn} defect.

While the NAC represents inelastic electron−phonon scattering that leads to energy exchange between the two subsystems, elastic scattering is characterized by the pure-dephasing times. Elastic scattering destroys correlation and the phase relationship between the electronic and vibrational subsystems. The pure-dephasing times are estimated based on the energy gap fluctuations using the second-order cumulant approximation of the optical response theory.[48−50] The pure-dephasing functions are shown in Figure 4. Gaussian fits to the functions are used to obtain the pure-dephasing times reported in Table 1. These are shorter in the presence of the defects. Thus, we conclude that the defects enhance both elastic and inelastic electron−phonon scattering in $CsSnI_3$.

After photoexcitation, the electron−phonon NAC promotes nonradiative recombination directly from the CBM to the VBM, as no midgap trap states are introduced, Figure 1. Figure 4(A) depicts the growth of the ground states populations in the pristine and defective systems due to the nonradiative transition. The carrier recombination times, τ, are estimated

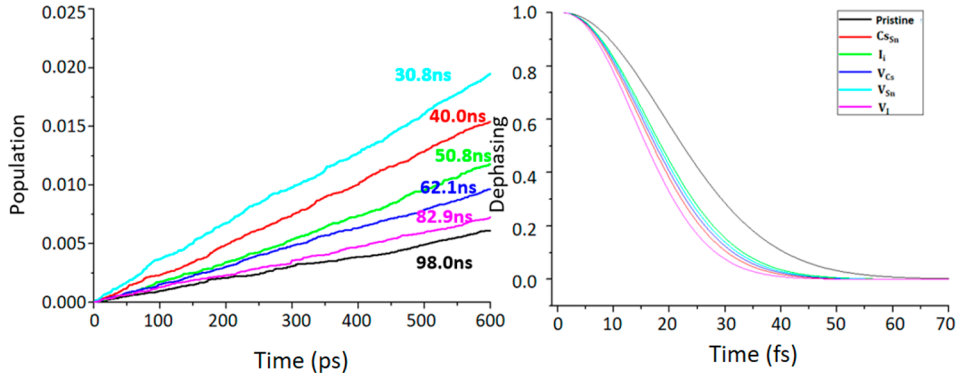

Figure 4. (A, left) Charge recombination process in pristine and defective $CsSnI_3$. The ecombination times are indicated by the numbers with the corresponding colors. (B, right) Pure-dephasing functions for the VBM-CBM transition in the $CsSnI_3$ systems. The pure-dephasing and recombination times are summarized in Table 1.

https://doi.org/10.1021/acs.jpclett.1c02443
J. Phys. Chem. Lett. 2021, 12, 8699−8705

with the short-time linear approximation to the exponential decay, $f(t) = \exp(-t/\tau) \approx 1 - t/\tau$. All defects accelerate the recombination, Table 1, although by a modest amount. The fastest recombination is observed for the V_{Sn} defect, which accelerates the recombination by a factor of 3 relative to pristine $CsSnI_3$. This defect creates the largest perturbation to the electronic subsystem, because it breaks many bonds in the Sn−I lattice that supports the charge carriers. The iodine vacancy causes the least acceleration. This is a favorable factor, since halide vacancies are very common in MHPs.[78−81] The iodine interstitial, which often accompanies creation of the iodine vacancy, cases an intermediate acceleration. The Cs vacancy has a minor effect, since Cs atoms do not contribute to the electron and hole wave functions. Replacing Sn with Cs has the second fastest e−h recombination, after the Sn vacancy. Thus, the defects associated with Sn atoms are most detrimental to the charge carrier lifetimes in $CsSnI_3$.

In summary, employing the time-dependent ab initio NA-MD simulation, we have investigated the nonradiative e−h recombination process in pristine and defective $CsSnI_3$. The investigated $CsSnI_3$ systems with the intrinsic point defects demonstrate no midgap trap states, indicating there are no deep charge recombination centers. Nevertheless, we observe moderate acceleration of the e−h recombination for all the defective systems as compared to pristine $CsSnI_3$. This is ascribed to the larger NAC arising from enhanced atomic motions in the perturbed crystal lattice. The largest, factor of 3, acceleration of the nonradiative charge recombination is seen in the systems with missing Sn atoms, including those with Sn vacancies and Sn replaced by Cs. This is because Sn atoms create the largest number of bonds, compared to Cs and I, and their removal generates the largest perturbation to the Sn−I lattice that supports the charge carriers. Cs and I vacancies are least detrimental to the charge carrier lifetimes, while iodine interstitial shows an intermediate effect.

Since point defects associated with I atoms are less detrimental than those associated with missing Sn atoms, it is advisable to carry out $CsSnI_3$ synthesis in Sn rich conditions. The reported study provides an atomistic rationalization of why lead-free $CsSnI_3$ exhibits a poorer performance compared to some lead-based perovskites. The insights from the NA-MD simulations contribute to our fundamental understanding of lead-free perovskites for solar energy applications, paving the way for improving the performance of lead-free perovskite materials.

■ ASSOCIATED CONTENT

Supporting Information

The Supporting Information is available free of charge at https://pubs.acs.org/doi/10.1021/acs.jpclett.1c02443.

Densities of states of the defect sites, Fourier transforms of autocorrelation functions of the energy gaps (PDF)

■ AUTHOR INFORMATION

Corresponding Author

Oleg V. Prezhdo − *Department of Chemistry, University of Southern California, Los Angeles, California 90089, United States;* orcid.org/0000-0002-5140-7500; Email: prezhdo@usc.edu

Authors

Yifan Wu − *Department of Chemistry, University of Southern California, Los Angeles, California 90089, United States*

Weibin Chu − *Department of Chemistry, University of Southern California, Los Angeles, California 90089, United States;* orcid.org/0000-0001-5951-0337

Andrey S. Vasenko − *HSE University, 101000 Moscow, Russia; I.E. Tamm Department of Theoretical Physics, P.N. Lebedev Physical Institute, Russian Academy of Sciences, 119991 Moscow, Russia;* orcid.org/0000-0002-2978-8650

Complete contact information is available at: https://pubs.acs.org/10.1021/acs.jpclett.1c02443

Notes

The authors declare no competing financial interest.

■ ACKNOWLEDGMENTS

The work was supported by the US National Science Foundation, grant No. CHE-1900510.

■ REFERENCES

(1) Chen, J. W.; Xu, X. H.; Tang, X. Y.; Jiang, T. M.; Chen, Z.; Ye, L.; Tian, Y.; Chen, X.; Liu, T. Y.; Su, Y. R.; et al. Highly Efficient and Thickness Insensitive Inverted Triple-Cation Perovskite Solar Cells Fabricated by Gas Pumping Method. *J. Phys. Chem. Lett.* **2021**, *12*, 5580−5586.

(2) Zhang, Z. J.; Jiang, Y.; Shu, M. Y.; Li, L.; Dong, Z. L.; Xu, J. Y. Artificial Photosynthesis over Metal Halide Perovskites: Achievements, Challenges, and Prospects. *J. Phys. Chem. Lett.* **2021**, *12*, 5864−5870.

(3) Best Research-Cell Efficiency Chart. https://www.nrel.gov/pv/cell-efficiency.html (Accessed on January 4, 2021).

(4) Ning, W.; Wang, F.; Wu, B.; Lu, J.; Yan, Z.; Liu, X.; Tao, Y.; Liu, J.-M.; Huang, W.; Fahlman, M.; et al. Long Electron−Hole Diffusion Length in High-Quality Lead-Free Double Perovskite Films. *Adv. Mater.* **2018**, *30*, 1706246.

(5) Stranks, S. D.; Eperon, G. E.; Grancini, G.; Menelaou, C.; Alcocer, M. J. P.; Leijtens, T.; Herz, L. M.; Petrozza, A.; Snaith, H. J. Electron-Hole Diffusion Lengths Exceeding 1 Micrometer in an Organometal Trihalide Perovskite Absorber. *Science* **2013**, *342*, 341−344.

(6) Oga, H.; Saeki, A.; Ogomi, Y.; Hayase, S.; Seki, S. Improved Understanding of the Electronic and Energetic Landscapes of Perovskite Solar Cells: High Local Charge Carrier Mobility, Reduced Recombination, and Extremely Shallow Traps. *J. Am. Chem. Soc.* **2014**, *136*, 13818−13825.

(7) Turren-Cruz, S.-H.; Saliba, M.; Mayer, M. T.; Juárez-Santiesteban, H.; Mathew, X.; Nienhaus, L.; Tress, W.; Erodici, M. P.; Sher, M.-J.; Bawendi, M. G. Enhanced Charge Carrier Mobility and Lifetime Suppress Hysteresis and Improve Efficiency in Planar Perovskite Solar Cells. *Energy Environ. Sci.* **2018**, *11*, 78−86.

(8) Yin, W.-J.; Shi, T.; Yan, Y. Unique Properties of Halide Perovskites as Possible Origins of the Superior Solar Cell Performance. *Adv. Mater.* **2014**, *26*, 4653−4658.

(9) Grancini, G.; Marras, S.; Prato, M.; Giannini, C.; Quarti, C.; De Angelis, F.; De Bastiani, M.; Eperon, G. E.; Snaith, H. J.; Manna, L.; et al. The Impact of the Crystallization Processes on the Structural and Optical Properties of Hybrid Perovskite Films for Photovoltaics. *J. Phys. Chem. Lett.* **2014**, *5*, 3836−3842.

(10) Chae, J.; Dong, Q.; Huang, J.; Centrone, A. Chloride Incorporation Process in Ch3nh3pbi3−X Cl X Perovskites Via Nanoscale Bandgap Maps. *Nano Lett.* **2015**, *15*, 8114−8121.

(11) Hao, F.; Stoumpos, C. C.; Chang, R. P. H.; Kanatzidis, M. G. Anomalous Band Gap Behavior in Mixed Sn and Pb Perovskites

Enables Broadening of Absorption Spectrum in Solar Cells. *J. Am. Chem. Soc.* **2014**, *136*, 8094−8099.
(12) Park, N.-G. Organometal Perovskite Light Absorbers toward a 20% Efficiency Low-Cost Solid-State Mesoscopic Solar Cell. *J. Phys. Chem. Lett.* **2013**, *4*, 2423−2429.
(13) Yu, H. L.; Wang, H. Y.; Zhang, T. K.; Yi, C.; Zheng, G. H. J.; Yin, C. Y.; Karlsson, M.; Qin, J. J.; Wang, J. P.; Liu, X. K.; et al. Color-Stable Blue Light-Emitting Diodes Enabled by Effective Passivation of Mixed Halide Perovskites. *J. Phys. Chem. Lett.* **2021**, *12*, 6041−6047.
(14) Li, H.; Pi, C. J.; Chen, W. Q.; Zhou, M.; Wei, J. M.; Yi, J. H.; Song, P.; Alexey, Y.; Zhong, Y.; Yu, X.; et al. A Highly Stable Photodetector Based on a Lead-Free Double Perovskite Operating at Different Temperatures. *J. Phys. Chem. Lett.* **2021**, *12*, 5682−5688.
(15) Huang, Y. Y.; Liang, C. Y.; Wu, D. F.; Chang, Q. J.; Liu, L. B.; Liu, H. B.; Tang, X. S.; He, Y.; Qiu, J. Surface Ligand Engineering for a Lead-Free Cs3cu2br5Microcrystal-Based Humidity Sensor with a Giant Response. *J. Phys. Chem. Lett.* **2021**, *12*, 3401−3409.
(16) Mosconi, E.; Azpiroz, J. M.; De Angelis, F. Ab Initio Molecular Dynamics Simulations of Methylammonium Lead Iodide Perovskite Degradation by Water. *Chem. Mater.* **2015**, *27*, 4885−4892.
(17) Grancini, G.; D'Innocenzo, V.; Dohner, E. R.; Martino, N.; Kandada, A. S.; Mosconi, E.; De Angelis, F.; Karunadasa, H. I.; Hoke, E. T.; Petrozza, A. Ch 3 Nh 3 Pbi 3 Perovskite Single Crystals: Surface Photophysics and Their Interaction with the Environment. *Chemical science* **2015**, *6*, 7305−7310.
(18) Giustino, F.; Snaith, H. J. Toward Lead-Free Perovskite Solar Cells. *ACS Energy Letters* **2016**, *1*, 1233−1240.
(19) Ke, W.; Kanatzidis, M. G. Prospects for Low-Toxicity Lead-Free Perovskite Solar Cells. *Nat. Commun.* **2019**, *10*, 965.
(20) Yang, S.; Fu, W.; Zhang, Z.; Chen, H.; Li, C.-Z. Recent Advances in Perovskite Solar Cells: Efficiency, Stability and Lead-Free Perovskite. *J. Mater. Chem. A* **2017**, *5*, 11462−11482.
(21) Li, W.; She, Y. L.; Vasenko, A. S.; Prezhdo, O. V. Ab Initio Nonadiabatic Molecular Dynamics of Charge Carriers in Metal Halide Perovskites. *Nanoscale* **2021**, *13*, 10239−10265.
(22) Wu, T. M.; Chen, X.; Wang, J. Metal-Free Hybrid Organic-Inorganic Perovskites for Photovoltaics. *J. Phys. Chem. Lett.* **2020**, *11*, 5938−5947.
(23) Shi, R.; Vasenko, A. S.; Long, R.; Prezhdo, O. V. Edge Influence on Charge Carrier Localization and Lifetime in Ch3nh3pbbr3 Perovskite: Ab Initio Quantum Dynamics Simulation. *J. Phys. Chem. Lett.* **2020**, *11*, 9100−9109.
(24) Wu, D. F.; Zhou, J. E.; Kang, W.; An, K.; Yang, J. Y.; Zhou, M.; He, P.; Huang, Q.; Tang, X. S. Ultrastable Lead-Free Csagcl2 Perovskite Microcrystals for Photocatalytic Co2 Reduction. *J. Phys. Chem. Lett.* **2021**, *12*, 5110−5114.
(25) Senocrate, A.; Spanopoulos, I.; Zibouche, N.; Maier, J.; Islam, M. S.; Kanatzidis, M. G. Tuning Ionic and Electronic Conductivities in the "Hollow" Perovskite {En}Mapbi(3). *Chem. Mater.* **2021**, *33*, 719−726.
(26) Kagan, C. R.; Mitzi, D. B.; Dimitrakopoulos, C. D. Organic-Inorganic Hybrid Materials as Semiconducting Channels in Thin-Film Field-Effect Transistors. *Science* **1999**, *286*, 945−947.
(27) Shum, K.; Chen, Z.; Qureshi, J.; Yu, C.; Wang, J.; Pfenninger, W.; Vockic, N.; Midgley, J.; Kenney, J. Synthesis and Characterization of Cssni3 Thin Films. *Appl. Phys. Lett.* **2010**, *96*, 221903.
(28) Chung, I.; Lee, B.; He, J.; Chang, R. P.; Kanatzidis, M. G. All-Solid-State Dye-Sensitized Solar Cells with High Efficiency. *Nature* **2012**, *485*, 486−9.
(29) Noel, N. K.; Stranks, S. D.; Abate, A.; Wehrenfennig, C.; Guarnera, S.; Haghighirad, A.-A.; Sadhanala, A.; Eperon, G. E.; Pathak, S. K.; Johnston, M. B.; et al. Lead-Free Organic−Inorganic Tin Halide Perovskites for Photovoltaic Applications. *Energy Environ. Sci.* **2014**, *7*, 3061−3068.
(30) Lee, B.; Stoumpos, C. C.; Zhou, N.; Hao, F.; Malliakas, C.; Yeh, C.-Y.; Marks, T. J.; Kanatzidis, M. G.; Chang, R. P. H. Air-Stable Molecular Semiconducting Iodosalts for Solar Cell Applications: Cs2sni6 as a Hole Conductor. *J. Am. Chem. Soc.* **2014**, *136*, 15379−15385.
(31) Shum, K.; Tsatskina, A. Solar Cells: Stabilizing Tin-Based Perovskites. *Nature Energy* **2016**, *1*, 16188.
(32) Lanzetta, L.; Webb, T.; Zibouche, N.; Liang, X.; Ding, D.; Min, G.; Westbrook, R. J. E.; Gaggio, B.; MacDonald, T. J.; Islam, M. S.; et al. Degradation Mechanism of Hybrid Tin-Based Perovskite Solar Cells and the Critical Role of Tin (Iv) Iodide. *Nat. Commun.* **2021**, *12*, 2853.
(33) Li, A. K.; Liu, Q.; Chu, W. B.; Liang, W. Z.; Prezhdo, O. V. Why Hybrid Tin-Based Perovskites Simultaneously Improve the Structural Stability and Charge Carriers' Lifetime: Ab Initio Quantum Dynamics. *ACS Appl. Mater. Interfaces* **2021**, *13*, 16567−16575.
(34) Ye, T.; Wang, X.; Wang, K.; Ma, S.; Yang, D.; Hou, Y.; Yoon, J.; Wang, K.; Priya, S. Localized Electron Density Engineering for Stabilized B-Γ Cssni3-Based Perovskite Solar Cells with Efficiencies > 10%. *ACS Energy Letters* **2021**, 1480−1489.
(35) Yu, C. L.; Chen, Z.; Wang, J. J.; Pfenninger, W.; Vockic, N.; Kenney, J. T.; Shum, K. Temperature Dependence of the Band Gap of Perovskite Semiconductor Compound Cssni3. *J. Appl. Phys.* **2011**, *110*, No. 063526.
(36) Rühle, S. Tabulated Values of the Shockley−Queisser Limit for Single Junction Solar Cells. *Sol. Energy* **2016**, *130*, 139−147.
(37) Shockley, W.; Queisser, H. J. Detailed Balance Limit of Efficiency of P-N Junction Solar Cells. *J. Appl. Phys.* **1961**, *32*, 510−519.
(38) Tvingstedt, K.; Malinkiewicz, O.; Baumann, A.; Deibel, C.; Snaith, H. J.; Dyakonov, V.; Bolink, H. J. Radiative Efficiency of Lead Iodide Based Perovskite Solar Cells. *Sci. Rep.* **2015**, *4*, 6071.
(39) Ball, J. M.; Petrozza, A. Defects in Perovskite-Halides and Their Effects in Solar Cells. *Nature Energy* **2016**, *1*, 16149.
(40) Chu, W.; Saidi, W. A.; Zhao, J.; Prezhdo, O. V. Soft Lattice and Defect Covalency Rationalize Tolerance of B-Cspbi3 Perovskite Solar Cells to Native Defects. *Angew. Chem., Int. Ed.* **2020**, *59*, 6435−6441.
(41) Li, W.; Liu, J.; Bai, F.-Q.; Zhang, H.-X.; Prezhdo, O. V. Hole Trapping by Iodine Interstitial Defects Decreases Free Carrier Losses in Perovskite Solar Cells: A Time-Domain Ab Initio Study. *ACS Energy Letters* **2017**, *2*, 1270−1278.
(42) He, J. L.; Vasenko, A. S.; Long, R.; Prezhdo, O. V. Halide Composition Controls Electron-Hole Recombination in Cesium-Lead Halide Perovskite Quantum Dots: A Time Domain Ab Lnitio Study. *J. Phys. Chem. Lett.* **2018**, *9*, 1872−1879.
(43) Xu, P.; Chen, S.; Xiang, H.-J.; Gong, X.-G.; Wei, S.-H. Influence of Defects and Synthesis Conditions on the Photovoltaic Performance of Perovskite Semiconductor Cssni3. *Chem. Mater.* **2014**, *26*, 6068−6072.
(44) Akimov, A. V.; Prezhdo, O. V. The Pyxaid Program for Non-Adiabatic Molecular Dynamics in Condensed Matter Systems. *J. Chem. Theory Comput.* **2013**, *9*, 4959−4972.
(45) Akimov, A. V.; Prezhdo, O. V. Advanced Capabilities of the Pyxaid Program: Integration Schemes, Decoherence Effects, Multi-excitonic States, and Field-Matter Interaction. *J. Chem. Theory Comput.* **2014**, *10*, 789−804.
(46) Jaeger, H. M.; Fischer, S.; Prezhdo, O. V. Decoherence-Induced Surface Hopping. *J. Chem. Phys.* **2012**, *137*, 22A545.
(47) Pal, S.; Trivedi, D. J.; Akimov, A. V.; Aradi, B.; Frauenheim, T.; Prezhdo, O. V. Nonadiabatic Molecular Dynamics for Thousand Atom Systems: A Tight-Binding Approach toward Pyxaid. *J. Chem. Theory Comput.* **2016**, *12*, 1436−1448.
(48) Akimov, A. V.; Prezhdo, O. V. Persistent Electronic Coherence Despite Rapid Loss of Electron−Nuclear Correlation. *J. Phys. Chem. Lett.* **2013**, *4*, 3857−3864.
(49) Habenicht, B. F.; Karnisaka, H.; Yamashita, K.; Prezhdo, O. V. Ab Initio Study of Vibrational Dephasing of Electronic Excitations in Semiconducting Carbon Nanotubes. *Nano Lett.* **2007**, *7*, 3260−3265.
(50) Hamm, P. *Principles of Nonlinear Optical Spectroscopy: A Practical Approach Or: Mukamel for Dummies*. University of Zurich, 2005; Vol. *41*, p 77.
(51) Kresse, G.; Furthmüller, J. Efficient Iterative Schemes for Ab Initio Total-Energy Calculations Using a Plane-Wave Basis Set. *Phys. Rev. B: Condens. Matter Mater. Phys.* **1996**, *54*, 11169−11186.

https://doi.org/10.1021/acs.jpclett.1c02443
J. Phys. Chem. Lett. 2021, 12, 8699−8705

(52) Perdew, J. P.; Burke, K.; Ernzerhof, M. Generalized Gradient Approximation Made Simple. *Phys. Rev. Lett.* **1996**, *77*, 3865−3868.
(53) Blöchl, P. E. Projector Augmented-Wave Method. *Phys. Rev. B: Condens. Matter Mater. Phys.* **1994**, *50*, 17953−17979.
(54) Chu, W.; Prezhdo, O. V. Concentric Approximation for Fast and Accurate Numerical Evaluation of Nonadiabatic Coupling with Projector Augmented-Wave Pseudopotentials. *J. Phys. Chem. Lett.* **2021**, *12*, 3082−3089.
(55) Chu, W. B.; Zheng, Q. J.; Akimov, A. V.; Zhao, J.; Saidi, W. A.; Prezhdo, O. V. Accurate Computation of Nonadiabatic Coupling with Projector Augmented-Wave Pseudopotentials. *J. Phys. Chem. Lett.* **2020**, *11*, 10073−10080.
(56) Wang, B. P.; Chu, W. B.; Tkatchenko, A.; Prezhdo, O. V. Interpolating Nonadiabatic Molecular Dynamics Hamiltonian with Artificial Neural Networks. *J. Phys. Chem. Lett.* **2021**, *12*, 6070−6077.
(57) Qiao, L.; Fang, W. H.; Long, R.; Prezhdo, O. V. Atomic Model for Alkali Metal Passivation of Point Defects at Perovskite Grain Boundaries. *Acs Energy Letters* **2020**, *5*, 3813−3820.
(58) Li, W.; Long, R.; Tang, J. F.; Prezhdo, O. V. Influence of Defects on Excited-State Dynamics in Lead Halide Perovskites: Time-Domain Ab Initio Studies. *J. Phys. Chem. Lett.* **2019**, *10*, 3788−3804.
(59) He, J. L.; Fang, W. H.; Long, R.; Prezhdo, O. V. Why Oxygen Increases Carrier Lifetimes but Accelerates Degradation of Ch3nh3pbi3 under Light Irradiation: Time-Domain Ab Initio Analysis. *J. Am. Chem. Soc.* **2020**, *142*, 14664−14673.
(60) Song, G.; Gao, B.; Li, G.; Zhang, J. First-Principles Study on the Electric Structure and Ferroelectricity in Epitaxial Cssni 3 Films. *RSC Adv.* **2017**, *7*, 41077−41083.
(61) Huang, L.-Y.; Lambrecht, W. Lattice Dynamics in Perovskite Halides Cssn X 3 with X = I, Br, Cl. *Phys. Rev. B: Condens. Matter Mater. Phys.* **2014**, *90*, 195201.
(62) Huang, L.-y.; Lambrecht, W. R. L. Zone-Center Phonons in Yellow Phase ${\Mathbf{Cssni}}_{3}$. *Physical Review Materials* **2017**, *1*, No. 024601.
(63) Kuok, M. H.; Tan, L. S.; Shen, Z. X.; Huan, C. H.; Mok, K. F. A Raman Study of Rbsnbr3. *Solid State Commun.* **1996**, *97*, 497−501.
(64) He, J.; Fang, W.-H.; Long, R. Unravelling the Effects of Oxidation State of Interstitial Iodine and Oxygen Passivation on Charge Trapping and Recombination in Ch3nh3pbi3 Perovskite: A Time-Domain Ab Initio Study. *Chemical Science* **2019**, *10*, 10079−10088.
(65) Kamisaka, H.; Kilina, S. V.; Yamashita, K.; Prezhdo, O. V. Ab Initio Study of Temperature- and Pressure Dependence of Energy and Phonon-Induced Dephasing of Electronic Excitations in Cdse and Pbse Quantum Dots. *J. Phys. Chem. C* **2008**, *112*, 7800−7808.
(66) Tong, C.-J.; Li, L.; Liu, L.-M.; Prezhdo, O. V. Long Carrier Lifetimes in Pbi2-Rich Perovskites Rationalized by Ab Initio Nonadiabatic Molecular Dynamics. *ACS Energy Letters* **2018**, *3*, 1868−1874.
(67) Chaban, V. V.; Prezhdo, V. V.; Prezhdo, O. V. Covalent Linking Greatly Enhances Photoinduced Electron Transfer in Fullerene-Quantum Dot Nanocomposites: Time-Domain Ab Initio Study. *J. Phys. Chem. Lett.* **2013**, *4*, 1−6.
(68) Li, L. Q.; Long, R.; Bertolini, T.; Prezhdo, O. V. Sulfur Adatom and Vacancy Accelerate Charge Recombination in Mos2 but by Different Mechanisms: Time-Domain Ab Initio Analysis. *Nano Lett.* **2017**, *17*, 7962−7967.
(69) Zhou, Z. H.; Liu, J.; Long, R.; Li, L. G.; Guo, L. J.; Prezhdo, O. V. Control of Charge Carriers Trapping and Relaxation in Hematite by Oxygen Vacancy Charge: Ab Initio Non-Adiabatic Molecular Dynamics. *J. Am. Chem. Soc.* **2017**, *139*, 6707−6717.
(70) Long, R.; Casanova, D.; Fang, W. H.; Prezhdo, O. V. Donor Acceptor Interaction Determines the Mechanism of Photoinduced Electron Injection from Graphene Quantum Dots into Tio2:Pi-Stacking Supersedes Covalent Bonding. *J. Am. Chem. Soc.* **2017**, *139*, 2619−2629.
(71) Zhang, Z. S.; Fang, W. H.; Tokina, M. V.; Long, R.; Prezhdo, O. V. Rapid Decoherence Suppresses Charge Recombination in Multi-Layer 2d Halide Perovskites: Time-Domain Ab Initio Analysis. *Nano Lett.* **2018**, *18*, 2459−2466.
(72) Zhao, Y. Y.; Zhou, S.; Zhao, J. J.; Du, Y.; Dou, S. X. Control of Photocarrier Separation and Recombination at Bismuth Oxyhalide Interface for Nitrogen Fixation. *J. Phys. Chem. Lett.* **2020**, *11*, 9304−9312.
(73) Antoniou, P.; Suchanek, F.; Varner, J. F.; Foley, J. J. Role of Cavity Losses on Nonadiabatic Couplings and Dynamics in Polaritonic Chemistry. *J. Phys. Chem. Lett.* **2020**, *11*, 9063−9069.
(74) Chen, Z.; Zhang, P. Z.; Zhou, Y.; Zhang, X. M.; Liu, X. R.; Hou, Z. F.; Tang, J. F.; Li, W. Elucidating the Influence of Sulfur Vacancies on Nonradiative Recombination Dynamics in Cu2znsns4 Solar Absorbers. *J. Phys. Chem. Lett.* **2020**, *11*, 10354−10361.
(75) Dou, W. Z.; Jia, Y. Z.; Hao, X. M.; Meng, Q. L.; Wu, J. G.; Zhai, S. W.; Li, T. Z.; Hu, W. J.; Song, B. Y.; Zhou, M. Time-Domain Ab Initio Insights into the Reduced Nonradiative Electron-Hole Recombination in Rese2/Mos2 Van Der Waals Heterostructure. *J. Phys. Chem. Lett.* **2021**, *12*, 2682−2690.
(76) Freixas, V. M.; White, A. J.; Nelson, T.; Song, H. J.; Makhov, D. V.; Shalashilin, D.; Fernandez-Alberti, S.; Tretiale, S. Nonadiabatic Excited-State Molecular Dynamics Methodologies: Comparison and Convergence. *J. Phys. Chem. Lett.* **2021**, *12*, 2970−2982.
(77) Park, W.; Lee, S.; Huix-Rotllant, M.; Filatov, M.; Choi, C. H. Impact of the Dynamic Electron Correlation on the Unusually Long Excited-State Lifetime of Thymine. *J. Phys. Chem. Lett.* **2021**, *12*, 4339−4346.
(78) Zhou, G. J.; Jia, X. F.; Guo, S. Q.; Molokeev, M.; Zhang, J. Y.; Xia, Z. G. Role of Halogen Atoms on High-Efficiency Mn2+ Emission in Two-Dimensional Hybrid Perovskites. *J. Phys. Chem. Lett.* **2019**, *10*, 4706−4712.
(79) Liu, Q.; Liang, W. Z. How the Structures and Properties of Pristine and Anion Vacancy Defective Organic-Inorganic Hybrid Double Perovskites Ma(2)Agin(Brxi1-X)(6) Vary with Br Content X. *J. Phys. Chem. Lett.* **2020**, *11*, 10315−10322.
(80) Li, W.; Zhan, J.; Liu, X. R.; Tang, J. F.; Yin, W. J.; Prezhdo, O. V. Atomistic Mechanism of Passivation of Halide Vacancies in Lead Halide Perovskites by Alkali Ions. *Chem. Mater.* **2021**, *33*, 1285−1292.
(81) Pols, M.; Vicent-Luna, J. M.; Filot, I.; van Duin, A. C. T.; Tao, S. X. Atomistic Insights into the Degradation of Inorganic Halide Perovskite Cspbi3: A Reactive Force Field Molecular Dynamics Study. *J. Phys. Chem. Lett.* **2021**, *12*, 5519−5525.

https://doi.org/10.1021/acs.jpclett.1c02443
J. Phys. Chem. Lett. 2021, 12, 8699−8705